Appl. Phys. A (2017) 123:510
DOI 10.1007/s00339-017-1122-z

Applied Physics A
Materials Science & Processing

Effects of thermal oxidation duration on the structural and electrical properties of Nd_2O_3/Si system

Karuppiah Hetherin[1] · S. Ramesh[1] · Yew Hoong Wong[1]

Received: 1 February 2017 / Accepted: 3 July 2017 / Published online: 10 July 2017
© Springer-Verlag GmbH Germany 2017

Abstract A study on the growth, structure and electrical properties of Nd_2O_3 was carried out experimentally on RF sputtered thin film on Si followed by thermal oxidation at 700 °C at different oxidation durations (5, 10, 15 and 20 min). The structural and chemical properties were studied by X-ray diffraction analysis, Fourier transform infrared analysis, Raman analysis and high resolution transmission electron microscopy analysis. The formation of cubic-Nd_2O_3, orthorhombic-$Nd_2Si_2O_7$, monoclinic-SiO_2, tetragonal-SiO_2 and hexagonal-SiO_2 was detected. A single interfacial layer was detected for the sample oxidized at 15 min and double interfacial layers were detected for the samples oxidized at 5, 10 and 20 min. The sample oxidized at 15 min possessed the best electrical properties which were attributed by the highest Nd_2O_3 intensity, largest SiO_2 crystallite structure, thinnest interfacial and oxide layer, highest barrier height, lowest effective oxide charges, slow trap density and average interface trap density.

Electronic supplementary material The online version of this article (doi:10.1007/s00339-017-1122-z) contains supplementary material, which is available to authorized users.

✉ Yew Hoong Wong
yhwong@um.edu.my

[1] Department of Mechanical Engineering, Faculty of Engineering, University of Malaya, 50603 Kuala Lumpur, Malaysia

1 Introduction

Silicon dioxide (SiO_2) has been utilized as a gate dielectric of field effect transistor [1]. It has good micro-processing capability, high dielectric breakdown, as well as thermal and electrical stability which have led to its survival so far. Technology demand limits the usage of SiO_2, where the leakage current is too high as its get thinner [2]. But, the effort of downscaling is necessary to continue Moore's law [3]. Thus, an alternative material is essential to replace SiO_2. The alternative thin material must be able to produce the same capacitance as SiO_2, at thicker layers [4].

A high dielectric constant (k) material will be a potential candidate to replace SiO_2. This material should be able to maintain high dielectric capacitance, while restraining gate leakage currents which is necessary for downscaled devices [5]. Several oxides have been investigated for the replacement. Initially, researchers focused on transition metals such as zirconium dioxide (ZrO_2) [6–8], hafnium dioxide (HfO_2) [8–11], tantalum pentoxide (Ta_2O_5) [12] and titanium dioxide (TiO_2) [8]. Common problems, faced by these high—k oxides, are formation of interfacial layer, micro-crystallization formation and phase separation, development of fixed charges within film and high density of interface states. These factors contribute to degradation of the electrical properties. However, properties of HfO_2 were improvised with nitrogen-doped Hf silicate. Nevertheless, the problem rises as it produces film with lower k value formation of interfacial layer with more than 10 nm. Additionally, this film is also difficult to scale for equivalent oxide thickness below 1 nm [13].

In recent years, researchers are focusing on rare earth oxides (REO) due to their excellent properties compared to other classes of materials. They possess a large band gap (4–6 eV), high resistivity (10^{12}–10^{15} Ωcm), high

crystallization temperatures, high relative permittivity (7–20), thermodynamic stability and most importantly have a high *k* value (7–20) [2, 4, 7, 14]. Additionally, a large bandgap produces deeper trapping levels for electron injected form substrates. Hence, this reduces the probability of back tunneling [15]. Even though the hygroscopic behaviors might form a hydroxide layer, there are some REOs such as lanthanum oxide (La_2O_3) and ytterbium(III) oxide (Yb_2O_3) which inhibit the formation of silica and silicide. At the same time, gadolinium(III) oxide (Gd_2O_3) stays chemically and electrically stable during annealing at a high temperature (850 °C) [16–18].

Neodymium oxide (Nd_2O_3) is one of the potential candidates from REO to replace SiO_2. It has a high *k* value (10–15), a large band gap of 5.8 eV and good lattice matching with Si. It is also thermodynamically stable when it comes in contact with Si, has good insulating properties and has the appropriate conduction band offset with Si which makes it suitable for microelectronic applications [19]. Moreover, there were no hydroxide layers or hydroxide elements found in any previous studies. So far, the oxide has been studied using various deposition methods such as atomic layer deposition (ALD) [20, 21], metalorganic chemical vapor deposition (MOCVD) [22], electron beam epitaxy (EBE) [4, 23] and reactive radio frequency (RF) sputtering [24, 25]. Each of these methods produced different results in terms of chemical, physical and electrical properties. These properties are strongly dependent on the precursor used, the growth cycle, the growth temperature and the growth ambient.

As reported earlier, it is important for an oxide to possess a Gibbs free energy (ΔG) of more than 0 kcal/mole when it comes in contact with Si, in order to prevent the formation of SiO_2 [12]. The calculated ΔG for SiO_2 and Nd silicide (NdSi) at 1000 K (727 °C) is as follows:

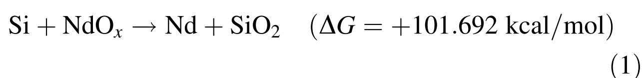

$$\mathrm{Si} + \mathrm{NdO}_x \rightarrow \mathrm{Nd} + \mathrm{SiO}_2 \quad (\Delta G = +101.692\ \mathrm{kcal/mol}) \tag{1}$$

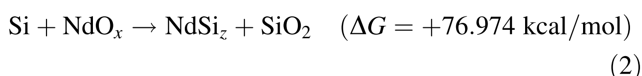

$$\mathrm{Si} + \mathrm{NdO}_x \rightarrow \mathrm{NdSi}_z + \mathrm{SiO}_2 \quad (\Delta G = +76.974\ \mathrm{kcal/mol}) \tag{2}$$

The equations indicate that Nd_2O_3 has thermal stability to resist the formation of SiO_2 and NdSi up to 727 °C.

In our recent studies, Nd_2O_3 was developed using the thermal oxidation method after the deposition of neodymium (Nd) by RF sputtering. This method is different compared to other research, since they involve direct Nd_2O_3 growth which is Nd sputtering in an O_2 ambient [15, 26–28]. With optimized parameters, this method may inhibit formation of the interfacial layers, since the substrate is not exposed to oxygen prior to metal deposition. However, silicide and silicate layers may form during oxidation at high temperatures. By considering the ΔG, the temperature of 700 °C is selected to study the effects of oxidation duration [25, 29].

2 Experimental

N-type Si(100) substrate, with a dimension of 1 cm × 1 cm, was cleaned using the standard Radio Corporation America (RCA) cleaning method before the deposition of Nd. This was followed by dipping in hydrofluoric acid (HF) (1 HF: 50 H_2O) for 10 s to remove the native oxide. Later, a deposition of a 10-nm Nd film was carried out by the physical vapor deposition (PVD) radio frequency (RF) sputtering system from Nd target (Kurt J. Lesker, USA, 99.9% purity). The base pressure, working pressure, RF power, distance between the substrate and target, and argon gas flow rate are as follows: 1.5×10^{-3} Pa, 3.0×10^{-3} Pa, 170 W, 20 cm, and 20 cm^3/min, respectively. Lastly, thermal oxidation was carried out upon sputtered Nd on Si, in Carbolite CTF tube furnace at 700 °C for different durations (5, 10, 15 and 20 min). The heating rate was 10 °C/min and upon reaching the desired temperature; the samples were heated at an oxygen gas flow rate of 150 mL/min. After they cooled down to room temperatures, they were removed from the furnace.

The physical and chemical properties of the films were determined by various characterizations. The crystallinity of the films was analyzed by a PANalytical Empyrean X-ray diffractometer (XRD) system at diffraction angles, 2θ, of 15°–90° with step time of 150 s and step size of 0.026°. Copper (Cu Kα) with wavelength (λ) of 0.154056 nm was employed by the system. Chemical functional groups were examined by Perkin Elmer Spectrum 400 Fourier transform infrared (FTIR) spectrometer. Meanwhile, the Horiba Xplora One Raman spectrometer was used to determine the chemical bonding stability and the TECNAI G2 F20 high resolution transmission electron microscope (HRTEM) was employed to evaluate the cross-section analysis of the films. Prior to evaluation, platinum (Pt) was deposited to protect the surface from bombardment damage caused by focused ion beam during lamella preparation. The chemical composition of the layers was detected by energy dispersive X-ray (EDX) through Oxford Instrument X-MaxN 80T SDD detector.

To proceed with current–voltage (*I*–*V*) and capacitance–voltage (*C*–*V*) measurements, MOS capacitors with $3 \times 3\ \mu m^2$ area were fabricated. At first, a 100-nm of aluminum (Al) was sputtered using TF450 PVD RF from Al target (Kurt J. Lesker, USA, 99.9995% purity) through a mask. Later, 100-nm Al film of Ohmic back contact was deposited on the backside of the substrate without the mask. The test was conducted using a BPW-800 8″ probe

station together with the Keithley 4200 semiconductor characterization system (SCS).

3 Result and discussion

3.1 XRD

Figure 1 shows the XRD patterns of the oxidized Nd samples at various durations (5, 10, 15 and 20 min). Two distinct peak peaks were observed at 33.0° and 69.0°. These peaks belong to the cubic (c)-Si (112) and c-Si (400). The peaks were confirmed based on the Inorganic Crystal Structure Database (ICSD) with a reference code of 98-001-6569.

Cubic (c)-Nd_2O_3 was detected at 68.8°, 74.9°, and 75.8°, corresponding to (118), (257), and (257), respectively. These peaks were confirmed based on ICSD 98-009-6204. Multiple phases of SiO_2 consisting of monoclinic (m), hexagonal (h), and tetragonal (t) were detected. Four peaks belonging to m-SiO_2 were detected at 46.2°, 47.8°, 54.6° and 89.4°, corresponding to (226), $(91\overline{3})$, $(51\overline{13})$ and (201). These peaks were confirmed by ICSD 98-001-0176 and ICSD 98-002-425. On the other hand, three peaks belonging to h-SiO_2 were detected at 69.4°, 75.3° and 75.6°, corresponding to (030), (104) and (302), respectively. These peaks were confirmed based on ICSD 98-001-6336, ICSD 98-001-6333 and ICSD 98-000-0174. In addition, a single peak belonging to t-SiO_2 was detected at 76.4°, corresponding to (040).These peaks were confirmed based on ICSD 98-000-9327. Meanwhile, five peaks belonging to an orthogonal (o)-$Nd_2Si_2O_7$ were detected at a diffraction angle of 55.4°, 56.3°, 61.8°, 66.5° and 67.4°, corresponding to (216), (313), (137), (160) and (208), respectively. These peaks were confirmed based on ICSD 98-001-6051. The findings of SiO_2 and $Nd_2Si_2O_7$ show the presence of an interfacial layer between the Si substrate and the oxide layer.

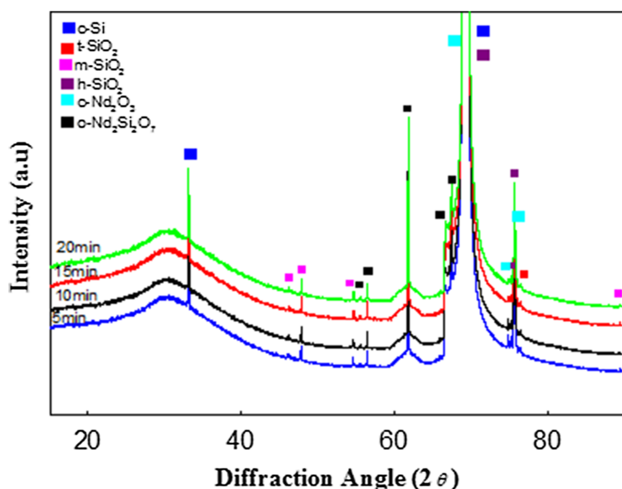

Fig. 1 XRD patterns of the oxidized Nd samples at various durations (5, 10, 15 and 20 min)

To determine the effects of oxidation duration on the interfacial layer, the highest intensities of c-Nd_2O_3, m-SiO_2, h-SiO_2, t-SiO_2 and o-$Nd_2Si_2O_7$ were investigated as shown in Fig. 2. The plot revealed that h-SiO_2 has the highest intensity, followed by c-Nd_2O_3. Meanwhile, the lowest intensity is t-SiO_2. The sample was oxidized at 15 min and the highest intensity for c-Nd_2O_3 and o-$Nd_2Si_2O_7$ was recorded. In addition, it showed the lowest intensity for m-SiO_2. The highest intensity of m-SiO_2 and t-SiO_2 was possessed by the sample oxidized for 10 min. Meanwhile, the sample oxidized at 20 min showed the highest intensity for h-SiO_2.

Williamson–Hall (W–H) analysis was employed to determine the crystalline sizes and microstrains for each element present in the XRD analysis [19, 30, 31]. Based on Debye–Scherrer, average nanocrystallite size is:

$$D = \frac{K\lambda}{\beta_D \cos\theta} \tag{3}$$

where D is the crystalline size, K is the shape factor which is a constant (0.9), λ is the wavelength of Cu Kα (0.1541 nm), β_D is the peak width with half maximum intensity and θ is the peak position. The strain induced due to distortion and crystal imperfection is given as:

$$\varepsilon = \frac{\beta_s}{4\tan\theta} \tag{4}$$

where β_s is the width at half maximum intensity. Combining Eqs. (1) and (2) gives rise to

$$\beta_{hkl} = \beta_D + \beta_s \tag{5}$$

$$\beta_{hkl} = \frac{K\lambda}{D\cos\theta} + 4\varepsilon\tan\theta \tag{6}$$

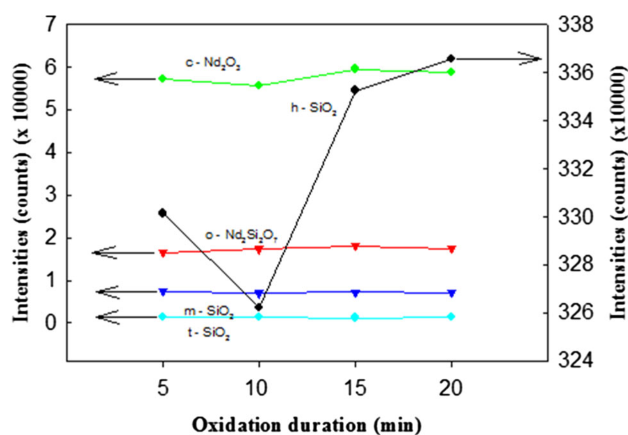

Fig. 2 Intensities of c-Nd_2O_3, m-SiO_2, h-SiO_2, t-SiO_2 and o-$Nd_2Si_2O_7$ for Nd-oxidized samples at various durations (5, 10, 15 and 20 min)

The rearrangement of Eq. (6) gives W–H equation as follows,

$$\beta_{\mathrm{hkl}}\cos\theta = \frac{K\lambda}{D} + 4\varepsilon\sin\theta \quad (7)$$

Graph of $\beta_{\mathrm{hkl}}\cos\theta$ against $\sin\theta$ was plotted for Nd_2O_3, SiO_2 and $Nd_2Si_2O_7$, respectively, as in Fig. 3.

From the linear fit data, D calculates from y-intercept which is $\frac{K\lambda}{D}$, and the ε calculated from the slope gradient. The method was employed to calculate D and ε values of Nd_2O_3, SiO_2 and $Nd_2Si_2O_7$, respectively. This analysis is vital as peaks broadening are due to crystallite size. This is caused by the finite size components diffracting incoherently with respect to one another. Meanwhile, broadening due to strain is caused by the non-uniform displacements of the atoms with respect to their reference-lattice positions [32]. These data provide value insight on to crystal defects [33]. Additionally, larger grain size will reduce number of electrical trapping site at grain boundary [34] and, thus, result in better electrical properties. Meanwhile, microstrain is related to grain boundary structure; as a result, it will also affect the electrical conductivity [35]. So, at larger grain size, the higher microstrain will be achieved. The microstrain and crystallite size are as shown in Fig. 4.

All the samples were negative for microstrain for all the compounds, except for the sample oxidized at 15 min for SiO_2. The samples oxidized at 5, 10 and 15 min showed the same microstrain value and crystallite size for Nd_2O_3. Additionally, the sample oxidized at 10 min showed the lowest microstrain value for both SiO_2 and $Nd_2Si_2O_7$. Meanwhile, the sample oxidized at 20 min had the lowest microstrain value and crystallite size of Nd_2O_3. On the other hand, the sample oxidized at 15 min showed the second highest value for both characteristics.

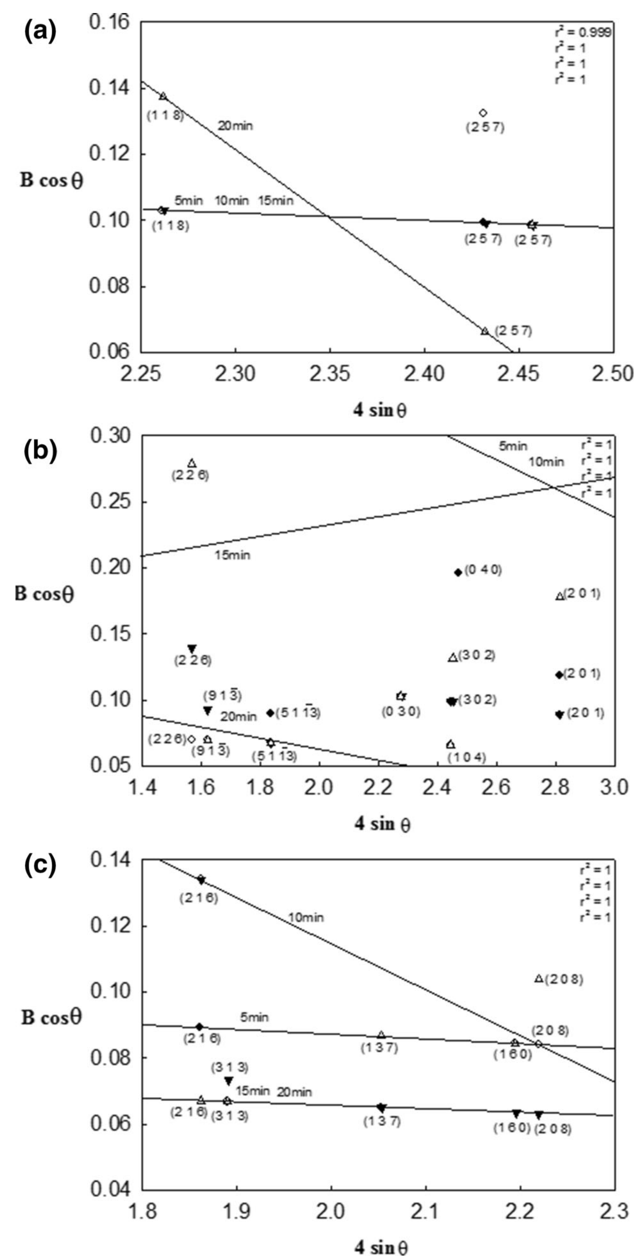

Fig. 3 W–H plot of **a** Nd_2O_3, **b** SiO_2, **c** $Nd_2Si_2O_7$ for Nd oxidized samples at various durations (5, 10, 15 and 20 min)

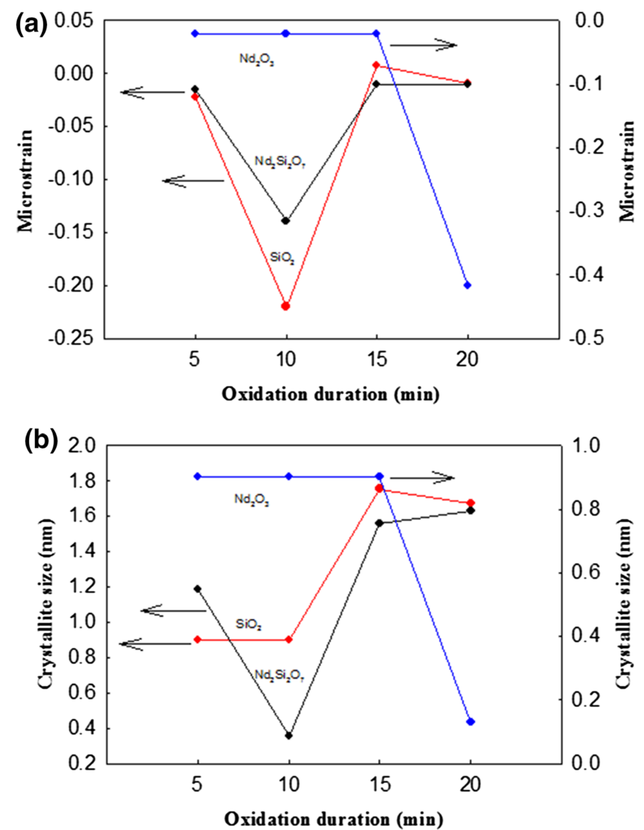

Fig. 4 **a** Microstrain, **b** crystallites size of Nd_2O_3, SiO_2, and $Nd_2Si_2O_7$ for Nd oxidized samples at various durations (5, 10, 15 and 20 min)

3.2 FTIR

The FTIR results for the samples are as shown in Fig. 5, with a scan range of 1300 cm^{-1} until 400 cm^{-1}. Si–Si vibration mode originating from Si substrate was detected at 613 cm^{-1} [36]. The peak broadens and until almost disappears at 20 min. Vibration mode that belongs to Nd–O was detected at 558 and 501 cm^{-1} [21]. Both peaks sharpened as oxidation duration increased. Si–O–Si asymmetric stretching mode was detected at 1204 cm^{-1} (refer to online resource Onl. Res. 1.) and 1041 cm^{-1} [37]. The peak at 1204 cm^{-1} broadened; meanwhile, the intensity of the peak at 1041 cm^{-1} increased as oxidation duration increased. The peak belonging to the rocking, bending and stretching of Si–O was detected at 805 cm^{-1} [36].

The Si–O vibration mode was detected at 478 and 471 cm^{-1} [38, 39]. The peak of 478 cm^{-1} sharpened as oxidation duration increased. Meanwhile, the peak at 471 cm^{-1} was only visible in the sample oxidized for 5 min. Additionally, Si–O mode was detected as Si–O–Si and Si–O bending mode. Si–O–Si bending was detected at 456 cm^{-1}. This peak sharpened when oxidation duration increased from 5 to 15 min. Later, at 20 min, it broadens. The peak belonging to the Si–O bend was detected at 443, 431, 419, 411 and 403 cm^{-1} [38, 39]. The peak of 443 cm^{-1} shifted at 5 and 10 min. Meanwhile, it sharpened at 15 min and decreased at 20 min. The peak of 431 cm^{-1} sharpened as oxidation duration increased. Meanwhile, the peak of 419 cm^{-1} was only visible for 15 min. On the other hand, the peak of 411 cm^{-1} was not visible for 15 min. This peak sharpened as oxidation duration increased from 5 to 10 min and later was visible at 20 min. Lastly, the peak of 403 cm^{-1} sharpened when the duration of oxidation increased from 5 to 10 min and decreased at 15 min. The last unknown peak at 925 cm^{-1} was assigned to Nd silicate vibration [36, 40]. Even though, the actual peak list is not available; it was confirmed based on other metal silicates such as hafnium silicate, zirconium silicate and samarium silicate. The peaks had almost negligible differences as the duration of oxidation increased.

3.3 Raman analysis

Figure 6 shows the Raman analysis result for the oxidized samples at various durations. The analysis was done from a wavelength of 0 cm^{-1} until 4000 cm^{-1}. Si wavelength was detected at 525 cm^{-1} [41]. The intensity decreased from 5 to 10 min. Later, it increased until 20 min. Two different peaks belonging to Nd_2O_3 were detected at 112 and 312 cm^{-1} [42]. Both peaks' intensity decreased until 15 min and then increased at 20 min. The peak of 925 cm^{-1} was assigned to SiO_2 [43]. The peak showed a similar trend as Nd_2O_3, where the intensity decreased until 15 min and increased at 20 min. Additionally, the unidentified peak at 17 cm^{-1} was assigned to neodymium silicate as it was detected in the XRD and FTIR analysis. The lowest intensity of silicate was at 5 min, followed by 15 and 20 min. The highest intensity was shown at 10 min. Raman's findings supported the existence of interfacial layers consisting of SiO_2 and $Nd_2Si_2O_7$.

3.4 HRTEM

The samples underwent HRTEM analysis to understand the effect of the duration of oxidation in the formation of oxide and interfacial layers. This step was essential to identify the influence of each layer's thickness in its electrical properties. Figure 7 shows the HRTEM analysis of the oxidized samples at various durations.

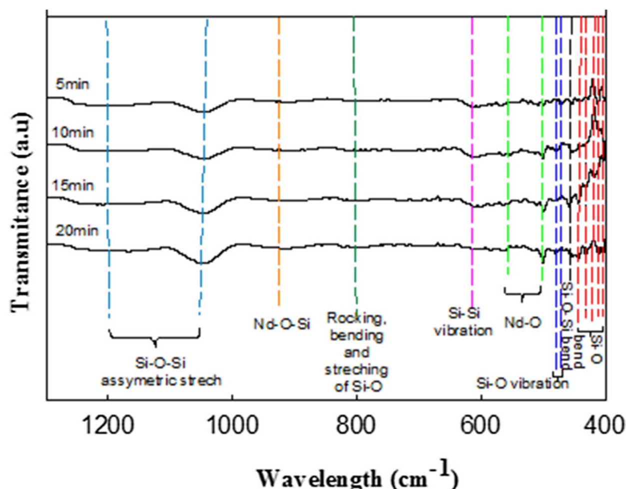

Fig. 5 FTIR spectra of the oxidized Nd samples at various durations (5, 10, 15 and 20 min)

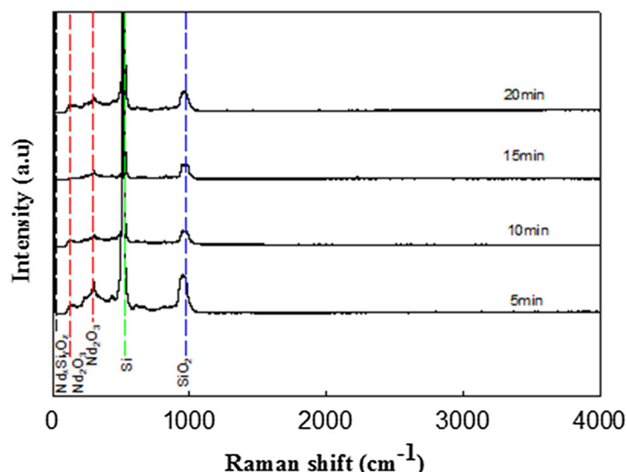

Fig. 6 Raman spectra of the oxidized Nd samples at various durations (5, 10, 15 and 20 min)

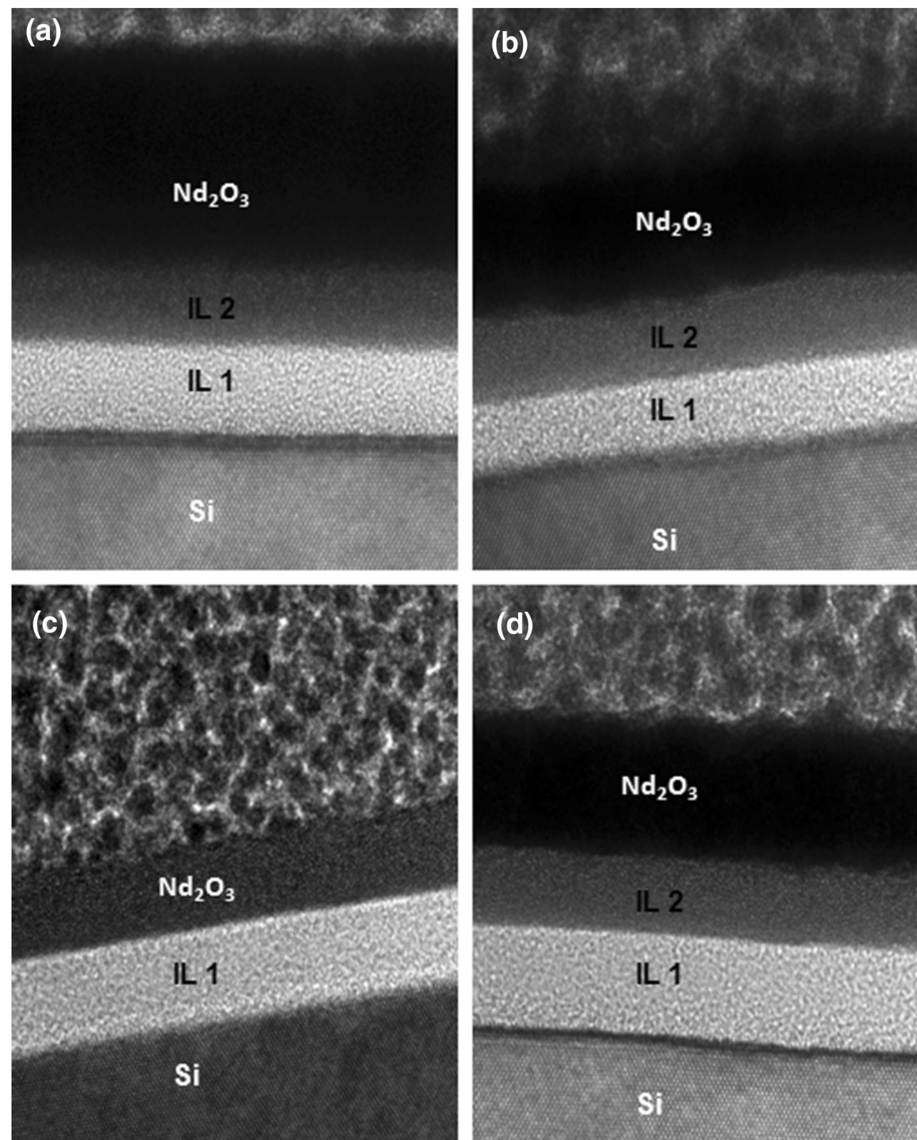

Fig. 7 HRTEM images of sample oxidized at **a** 5 min, **b** 10 min, **c** 15 min, **d** 20 min

Layers were observed in between oxide and Si substrate as shown by XRD, FTIR and Raman. First and foremost, the distinct differentiation can be observed for the sample oxidized at 15 min. It consists of the thinnest oxide layer and a single interfacial layer. Meanwhile, the rest of the samples consists of two interfacial layers. To understand the thickness variation, the thickness of each layer was plotted as shown in Fig. 8.

The oxide layer showed thickness reduction until 15 min and increased at 20 min. The first interfacial layer increased until 15 min and then decreased at 20 min. Meanwhile, the second interfacial layer decreased until 15 min and did not exist at 15 min but the layer appeared again at 20 min. The interfacial layer at 15 min was thicker than the oxide layer. Based on these findings, an oxidation model is proposed as shown in Fig. 9.

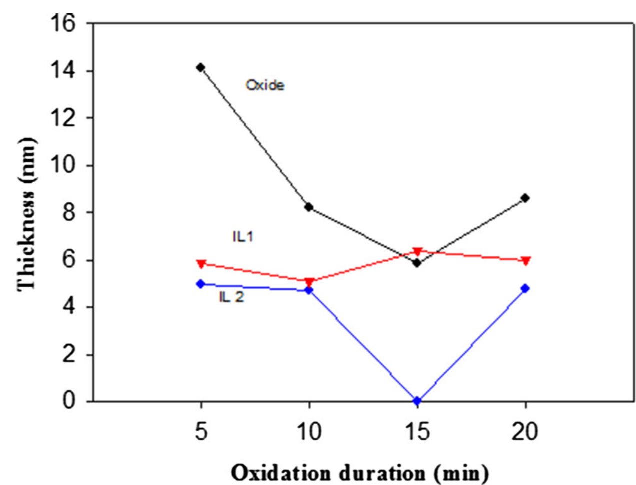

Fig. 8 Thickness variation of each layer by oxidation durations

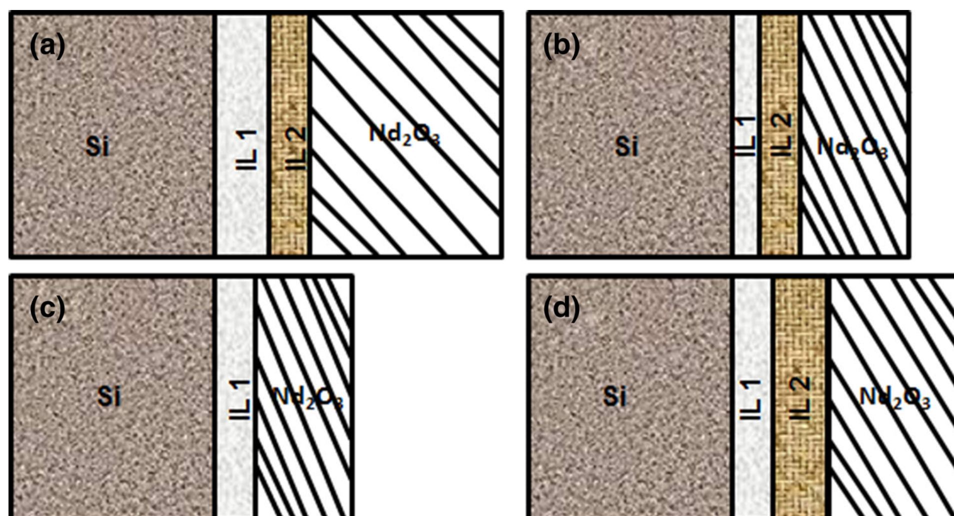

Fig. 9 Model of layers distribution for different oxidation durations. **a** 5 min, **b** 10 min, **c** 15 min, **d** 20 min

Table 1 Compound of interfacial layers by durations

Oxidation duration (min)	Oxide layer	IL 1	IL 2
5	Nd_2O_3	SiO_2	$Nd_2Si_2O_7$
10	Nd_2O_3	SiO_2	$Nd_2Si_2O_7$
15	Nd_2O_3	$SiO_2 + Nd_2Si_2O_7$	Does not exist
20	Nd_2O_3	SiO_2	$Nd_2Si_2O_7$

At the initial oxidation state, the oxidation occurred at a higher rate at 0.047 nm/s. Thus, the thickest oxide layer is formed at 5 min. From XRD, FTIR and Raman analysis, it is known that the interfacial layer consists of SiO_2 and $Nd_2Si_2O_7$. Thus, it can be assumed that the interfacial layer closest to Si is made of SiO_2 [23, 30] as the oxygen atoms diffuse in and combine with Si. Meanwhile, the second interfacial layer consists of $Nd_2Si_2O_7$ as the Nd atoms also diffuse in at the same time the oxygen atoms diffuse in. Meanwhile, the Si atoms diffused out and formed $Nd_2Si_2O_7$ [44]. Based on this model, the compound present in each element is shown in Table 1. The thickness of these layers decreased at 10 min, possibly due to the longer oxidation duration. At this duration, the oxidation level is lowered and the diffusion of atoms is reduced due to the consolidation of crystal atoms. The applied thermal energy leads to a sintering effect; thus, atoms become more compact [45]. At 15 min, the duration is optimized and only a single interfacial layer can be obtained. The atoms are more compact at this duration than at 10 min. This amorphous region consists of a mixture of SiO_2 and $Nd_2Si_2O_7$. As the diffusion rate and the oxidation rate decrease, the total thickness is not very different than the original thickness (10 nm of Nd). It can scavenge the formation of the SiO_2 and $Nd_2Si_2O_7$ interfacial layers separately. But as the oxidation duration increases to 20 min, the oxide and interfacial layer's thickness start to increase again and higher than 10 min. After consolidation of atoms at 15 min, the oxidation rate increases due to longer oxidation time at 20 min. As a result, the thickness increases since there is more oxygen availability to form bonding. A reverse effect can be seen, where the consolidation of atoms becomes less pronounced.

3.5 *J–E* measurement

I–V data were employed to obtain leakage current density–electric field (*J–E*) as shown in Fig. 10.

The *E* value obtained from

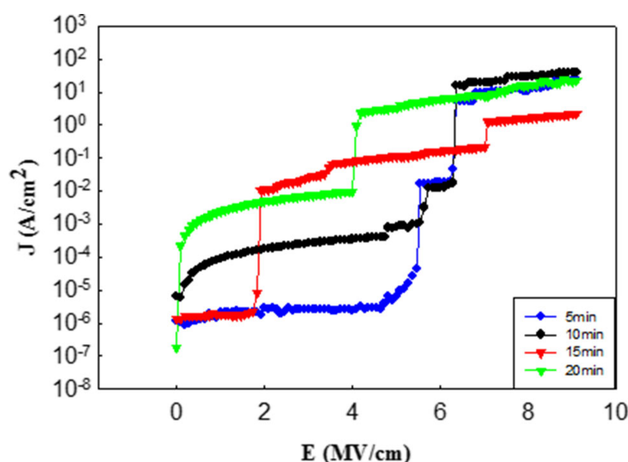

Fig. 10 *J–E* characteristics of the oxidized Nd samples at various durations (5, 10, 15 and 20 min)

Table 2 Electrical result comparison of previously published works

Method	Oxide	IL	Thickness (nm)	*E* (MV/cm)	*J* (A/cm^2)	References
Metal organic chemical vapour deposition	Nd_2O_3	$Nd_2Si_2O_7$	35	1.4	10^{-4}	[55]
Chemical solution deposition	Nd_2O_3	SiO_2	3.3	Not reported	10^{-4}	[56]
RF sputtering	Nd_2O_3	N^+Poly-Si and wet oxide	27	3	10^{-4}	[57]
RF sputtering	Nd_2O_3	N^+Poly-Si and wet oxide	25	11	10^{-4}	[49]
RF sputtering followed by thermal oxidation	Nd_2O_3	$SiO_2 + Nd_2Si_2O_7$	5.82–14.1	1.8	10^{-6}	This work

$$E = \frac{(V_g - V_{fb})}{t_{ox}} \tag{8}$$

The samples possess double breakdowns. The initial breakdown at the lower *E* value is the soft breakdown. The later breakdown at the higher *E* value is the hard breakdown. The samples oxidized at 10 and 20 min started with leakage, thus concluding both as having the worst electrical characteristics. This could be attributed to the almost similar oxide thickness of 8.21 and 8.6 nm, respectively. The initial breakdown of the sample oxidized at 15 min is at 1.818 MV/cm and 8.118 × 10^{-6} A/cm^2. Meanwhile, for the sample oxidized at 5 min, the initial breakdown was at 5.4545 MV/cm and 4.178 × 10^{-5} A/cm^2. Thus, the sample oxidized at 15 min is thought to have better electrical properties due to a lower *J* value. This can be attributed due to its single interfacial layer, which is the thinnest interfacial layer at 6.38 nm. Jeon et al. have reported that the sample with the thinnest interfacial layer possessed better electrical properties [46]. Moreover, a thick oxygen-rich layer such as SiO_2 has a strong effect on the electrical properties on the samples oxidized at 5, 10 and 20 min, since the *k* value of this oxide is ~3.9 [23, 47]. Table 2 shows a comparison of previously published results for Nd_2O_3.

The results indicate that sample with SiO_2 produces poor result compared to sample with silicate as interface layer. From *J*–*E* measurements, time-zero dielectric breakdown (TZDB) reliability tests had been performed. A total of 40 capacitors were tested and cumulative failure percentage of the breakdown is as shown in Fig. 11.

The highest breakdown voltage was recorded in the range of 3–5 MV/cm for the sample oxidized at 5 and 10 min. But the leakage values recorded were higher than 10^{-6} A/cm^2. Thus, 1.8 MV/cm is assumed to be the best based on the fact that it corresponds to the lowest leakage value. Interface layer with inclusion of $Nd_2Si_2O_7$ and SiO_2 has the best *J*–*E* result. This is vice versa with the observation of samarium silicate interface layer, where it degrades the electrical properties of the oxide film [48].

The Fowler–Nordheim (FN) type current conduction is one the accepted mechanisms that result in current conduction in thin gate oxide [21]. In this type of leakage, the carrier tunnels through a triangular barrier into the conduction, the valence band of the insulator F–N tunneling is characterized by the barrier which is triangular and tunneling is only through insulator layer [49].

The data of *J*–*E* employed to perform F–N tunneling linear regression plot and barrier height (ϕ_B) between conduction band edge between Si and interface from it.

$$\left(J_{FN} = AE^2 \exp\left(-\frac{B}{E}\right)\right) \tag{9}$$

where

$$A = 1.54 \times 10^{-6}\left(\frac{m}{m_{ox}}\right)\phi_B \tag{10}$$

$$B = 6.83 \times 10^7\left(\frac{m_{ox}}{m}\right)(\phi_B^3)^{\frac{1}{2}} \tag{11}$$

Rearranging Eq. (9) gives rise to the following equation:

$$\ln\left(\frac{J}{E^2}\right) = -B\left(\frac{1}{E}\right) + \ln A \tag{12}$$

Figure 12 shows the FN tunneling linear regression plot of the oxidized Nd samples at various durations (5, 10, 15 and 20 min). Based on the linear equation, the *y*-intercept is equal to *A* and the gradient is equal to *B*. Meanwhile, the effective mass of high *k* is assumed to be 0.3 m for calculation [50]. The result of the barrier height is as shown in

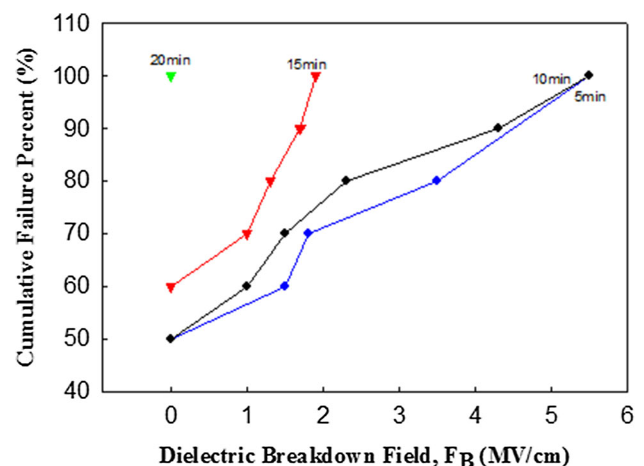

Fig. 11 Cumulative failure percentage of dielectric breakdown field of investigated samples

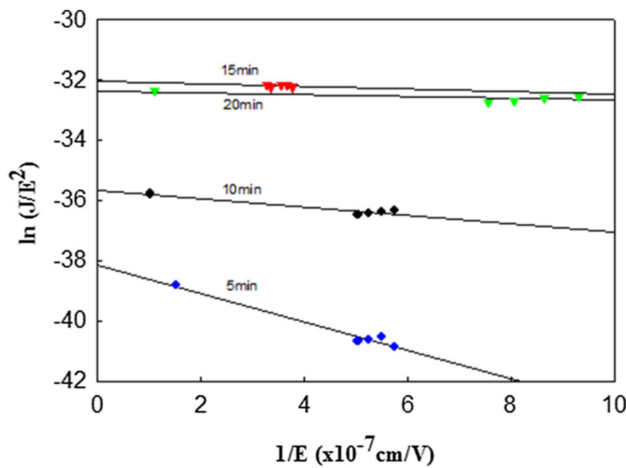

Fig. 12 FN tunneling linear regression plot of the oxidized Nd samples at various durations (5, 10, 15 and 20 min)

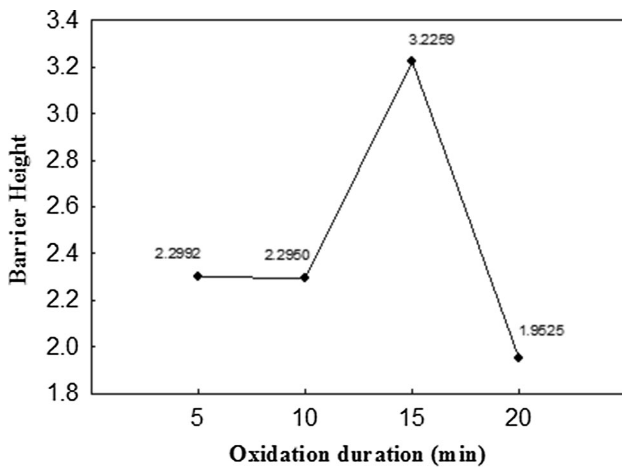

Fig. 13 Barrier height of the oxidized Nd samples at various durations (5, 10, 15 and 20 min)

Fig. 13. The sample with highest (ϕ_B) has the best electrical properties, which is 15 min.

3.6 *C–V* characteristics

Figure 14 shows the capacitance accumulation and *k* value of oxidized Nd samples at various durations. Measurement had been done within the bias voltage ranging from −8 to +2 V.

Sample oxidized at 20 min possess the highest accumulation capacitance. Meanwhile, the lowest accumulation capacitance shown by sample oxidized at 15 min. This trend is vice versa with *J–E* analysis. $C_{Nd_2O_3}$ is obtained from [42, 51],

$$C = \frac{kA\epsilon_0}{t} \quad (13)$$

where C is the capacitance of the oxide, k is the effective dielectric constant, A is the area of capacitor, ϵ_0 is the

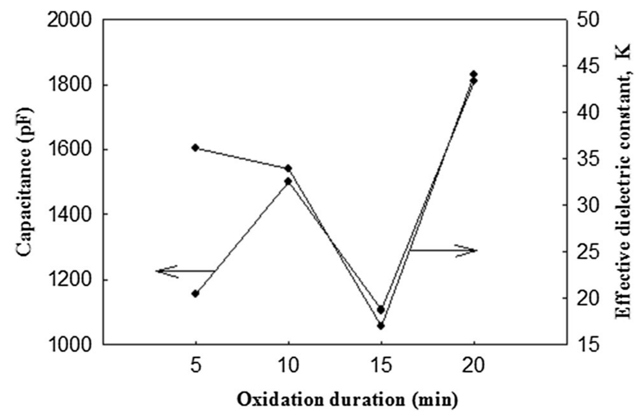

Fig. 14 Capacitance accumulation and *k* value of oxidized Nd samples at various durations (5, 10, 15 and 20 min)

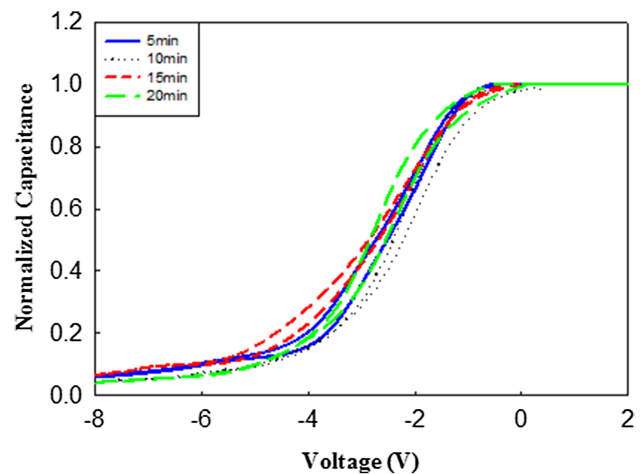

Fig. 15 Normalized *C–V* curved at room temperature of oxidized Nd samples at various durations (5, 10, 15 and 20 min)

permittivity of free space (8.85×10^{-12} Fm^{-1}) and t is the thickness of the oxide film. Based on the equation, C is directional proportional to k and inversely proportional to t. These two factors highly influence the C value, as A and ε_0 are constant. Based on the Eq. 13, sample with lowest capacitance accumulation and thickness possess the lowest k. The 15-min sample that has interface layer with inclusion of $Nd_2Si_2O_7$ and SiO_2 gives the lowest k value. Even the value is lower compared to other samples, it is higher compared to previous published result, where for thickness less than 25 nm, the k value is 13 ± 2 [46].

C–V result was further analyzed by normalized the capacitance value with accumulation capacitance of each sample as shown in Fig. 15.

The result indicates negative bias depletion region and negatively shifted flatband voltage (ΔV_{FB}). Thus, oxide of all the samples possesses positive effective oxide charges [52]. The effective oxide charges (Q_{eff}) and slow trap

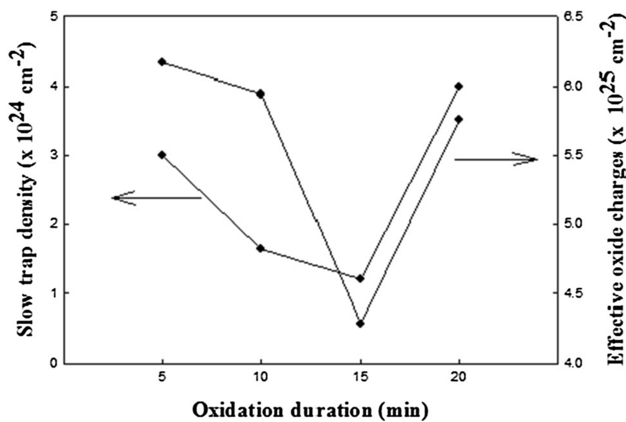

Fig. 16 Slow trap density and effective oxide charges of oxidized Nd samples at various durations (5, 10, 15 and 20 min)

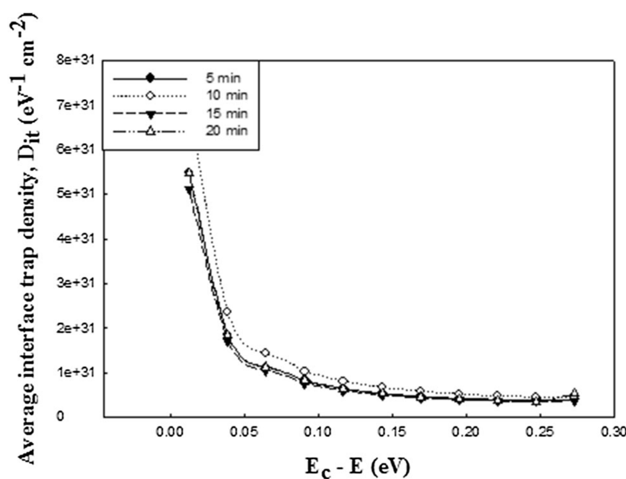

Fig. 17 The average interface trap density of oxidized Nd samples at various durations (5, 10, 15 and 20 min)

density (STD) of the samples were calculated based on the equations below [53, 54]:

$$Q_{\mathrm{eff}} = \frac{C_{\mathrm{ox}}\Delta V_{\mathrm{FB}}}{qA} \tag{14}$$

$$\mathrm{STD} = \frac{\Delta V C_{\mathrm{ox}}}{qA} \tag{15}$$

where q is the electronic charge (1.6×10^{-19} C), ΔV is the difference between flatband voltages of hysteresis curve and other parameters have been explained previously. The calculated Q_{eff} and STD are as shown in Fig. 16.

Sample oxidized for 15 min shows the lowest values for both Q_{eff} and STD. Both Q_{eff} and STD show similar trend as the interfacial layer thickness, where the highest interfacial layer has the highest Q_{eff} and STD.

The average interface trap density was calculated using Terman method as in equation below [51, 53]:

$$D_{\mathrm{it}} = \frac{\Delta V_{\mathrm{g}} C_{\mathrm{ox}}}{\phi_{\mathrm{s}} qA} \tag{16}$$

where (ϕ_{s}) is the surface potential of Si at specific gate voltage, V_{g}. The surface potential of a particular capacitance is taken from an ideal MOS capacitor. The gate voltage is obtained from experimental *C*–*V* curve of the same capacitance as that of (ϕ_{s}). The steps were then repeated for other data points until a relevant D_{it} against ($E_{\mathrm{c}} - E$) curve is obtained. Figure 17 shows the average interface trap density. Sample oxidized for 15 min possesses the lowest average interface trap density. This supported by Pan et al.'s finding where the D_{it} tends to increase with SiO_2 and silicate layer [31].

4 Conclusion

In summary, the work demonstrated the effect of the duration of thermal oxidation (5, 10, 15 and 20 min) of sputtered Nd on Si with regard to structural, chemical and electrical properties. The XRD, FTIR and Raman result showed the presence of the interfacial layers of Si–O and Nd–Si–O in between Si and Nd_2O_3. Additionally, HRTEM analysis showed two distinct interfacial layers for the samples oxidized at 5, 10 and 20 min and a single interfacial layer for the sample oxidized at 15 min. With the attainment of thinnest interfacial and oxide layer, highest barrier height, highest Nd_2O_3 intensity, largest SiO_2 crystallite structure, effective oxide charges, slow trap density and average interface trap density, this 15-min sample produced the best electrical properties, which demonstrated the highest electrical breakdown field with the lowest leakage current density.

Acknowledgements This work was supported by University of Malaya through Postgraduate Research Grant (PPP) [PG028-2015A] and Ministry of Higher Education, Malaysia through Fundamental of Research Grant Scheme (FRGS) [FRGS/1/2016/STG07/UM/02/6].

References

1. R.A. McKee, F.J. Walker, M.F. Chisholm, Phys. Rev. Lett. **81**(14), 3014 (1998)
2. P. Zaumseil, T. Schroeder, J. Phys. D Appl. Phys. **38**(10A), A179 (2005)
3. Apurba Laha, A. Fissel, H.J. Osten, Appl. Phys. Lett. **102**(20), 202902 (2013)
4. A.A. Dakhel, physica status solidi (a) **201**(4), 745 (2004)
5. J. Kang, D.Y. Kim, K.J. Chang, J. Korean Phys. Soc. **50**(3), 552 (2007)
6. V.V. Atuchin, V.N. Kruchinin, Y.H. Wong, K.Y. Cheong, Mater. Lett. **105**, 72 (2013)
7. G.D. Wilk, R.M. Wallace, J.M. Anthony, J. Appl. Phys. **89**(10), 5243 (2001)
8. Y.H. Wong, K.Y. Cheong, Thin Solid Films **520**, 6822 (2012)

9. C. Hobbs, H. Tseng, K. Reid, B. Taylor, L. Dip, L. Hebert, R. Garcia, R. Hegde, J. Grant, D. Gilmer, A. Franke, V. Dhandapani, M. Azrak, L. Prabhu, R. Rai, S. Bagchi, J. Conner, S. Backer, F. Dumbuya, B. Nguyen, P. Tobin, Presented at the Electron Devices Meeting, 2001. IEDM '01. Technical Digest. International, 2001 (unpublished)
10. K. Shiraishi, K. Yamada, K. Torii, Y. Akasaka, K. Nakajima, M. Konno, T. Chikyow, H. Kitajima, T. Arikado, Jpn. J. Appl. Phys. **43**(11A), L1413 (2004)
11. K. Xiong, P.W. Peacock, J. Robertson, Appl. Phys. Lett. **86**(1), 012904 (2005)
12. T. Dimitrova, E. Atanassova, Solid-State Electron. **42**(3), 307 (1998)
13. K. Kakushima, K. Tsutsui, S.-I. Ohmi, P. Ahmet, V. Rao, H. Iwai, Rare Earth Oxide Thin Films **106**, 345 (2007)
14. A.A. Dakhel, J. Alloy. Compd. **376**(1), 38 (2004)
15. T.-M. Pan, J.-C. Lin, Sens. J. IEEE **9**(10), 1173 (2009)
16. J. Kwo, M. Hong, A.R. Kortan, K.L. Queeney, Y.J. Chabal, R.L. Opila, D.A. Muller, S.N.G. Chu, B.J. Sapjeta, T.S. Lay, J. Appl. Phys. **89**, 3920 (2001)
17. L. Marsella, V. Fiorentini, Phys. Rev. B **69**(17), 172103 (2004)
18. Y. Zhao, Materials **5**(8), 1413 (2012)
19. X. Fan, H. Liu, X. Zhang, Appl. Phys. A **114**(2), 545 (2014)
20. A. Kosola, J. Päiväsaari, M. Putkonen, L. Niinistö, Thin Solid Films **479**(1), 152 (2005)
21. J. Päiväsaari, M. Putkonen, L. Niinistö, Thin Solid Films **472**(1), 275 (2005)
22. K. Frohlich, R. Luptak, E. Dobrocka, K. Husekova, K. Cico, A. Rosova, M. Lukosius, A. Abrutis, P. Pisecny, J.P. Espinos, Mater. Sci. Semicond. Process. **9**(6), 1065 (2006)
23. E. Bugiel, H.J. Osten, A. Fissel, O. Kirfel, M. Czernohorsky, in *Microscopy of Semiconducting Materials*, vol. 107, ed. by A.G. Cullis, J.L. Hutchison (Springer, Berlin, 2005), p. 343
24. C.H. Kao, H. Chen, Y.-C. Liao, J.Z. Deng, Y.C. Chu, Y.T. Chen, H.W. Chang, Thin Solid Films **570**, 412 (2014)
25. T.-M. Pan, C.-C. Huang, Appl. Surf. Sci. **256**(23), 7186 (2010)
26. T.-M. Pan, J.-D. Lee, W.-H. Shu, T.-T. Chen, Appl. Phys. Lett. **89**(23), 2908 (2006)
27. T.-M. Pan, C.-W. Lin, J.-C. Lin, S.-H. Su, H.-M. Kuo, Y.-K. Chien, Presented at the Sensors, 2009 IEEE (2009) (unpublished)
28. T.-M. Pan, T.-Y. Yu, Semicond. Sci. Technol. **24**(9), 095022 (2009)
29. K. Kuroiwa, T. Ueno, M. Hasumi, Y. Iwazaki, Y. Oniki, Presented at the Meeting Abstracts, 2008 (unpublished)
30. A. Laha, A. Fissel, E. Bugiel, H.J. Osten, Thin Solid Films **515**(16), 6512 (2007)
31. T.-M. Pan, J.-D. Lee, W.-W. Yeh, J. Appl. Phys. **101**(2), 024110 (2007)
32. A.R. Bushroa, R.G. Rahbari, H.H. Masjuki, M.R. Muhamad, Vacuum **86**(8), 1107 (2012)
33. K.H. Goh, A.S.M.A. Haseeb, Y.H. Wong, Thin Solid Films **606**, 80 (2016)
34. H. Zeng, Y. Wu, J. Zhang, C. Kuang, M. Yue, S. Zhou, Prog Nat Sci Mater Int **23**(1), 18 (2013)
35. J.M. Tao, M.C. Xu, C.J. Li, X.K. Zhu, Mater. Technol. **27**(1), 82 (2012)
36. B.C. Smith, *Infrared Spectral Interpretation: A Systematic Approach* (Taylor & Francis, London, 1998)
37. T. Kurniawan, K.Y. Cheong, K.A. Razak, Z. Lockman, N. Ahmad, J. Mater. Sci. Mater. Electron. **22**(2), 143 (2011)
38. E.R. Lippincott, A. Van Valkenburg, C.E. Weir, E.N. Bunting, J. Res. Natl. Bur. Stand. **61**(1), 61 (1958)
39. C.E. Viana, A.N.R. da Silva, N.I. Morimoto, Braz. J. Phys. **31**, 299 (2001)
40. M. Ganesan, M.V.T. Dhananjeyan, K.B. Sarangapani, N.G. Renganathan, J. Alloy. Compd. **450**(1), 452 (2008)
41. Y.H. Wong, K.Y. Cheong, J. Alloy. Compd. **509**(35), 8728 (2011)
42. T. Kurniawan, K.Y. Cheong, K.A. Razak, Z. Lockman, N. Ahmad, J. Mater. Sci. Mater. Electron. **22**(2), 143 (2011)
43. R.A. Nyquist, R.O. Kagel, *Handbook of Infrared and Raman Spectra of Inorganic Compounds and Organic Salts: Infrared Spectra of Inorganic Compounds* (Academic, London, 2012)
44. S. Jayanti, X. Yang, D.J. Lichtenwalner, V. Misra, Appl. Phys. Lett. **96**, 092905 (2010)
45. S.J.L. Kang, *Sintering: Densification, Grain Growth and Microstructure* (Elsevier Science, Amsterdam, 2004)
46. S. Jeon, K. Im, H. Yang, H. Lee, H. Sim, S. Choi, T. Jang, H. Hwang, Presented at the Electron Devices Meeting, 2001. IEDM'01. Technical Digest. International, 2001 (unpublished)
47. G. Lucovsky, G.B. Rayner, Appl. Phys. Lett. **77**(18), 2912 (2000)
48. K.H. Goh, A.S.M.A. Haseeb, Y.H. Wong, J. Electron. Mater. **45**(10), 5302 (2016)
49. A.A. Demkov, A. Navrotsky, *Materials Fundamentals of Gate Dielectrics* (Springer, Berlin, 2006)
50. M. Salmani-Jelodar, H. Ilatikhameneh, S.G. Kim, K. Ng, G. Klimeck, (2015). arXiv:1502.06178 **(preprint)**
51. K.H. Goh, A.S.M.A. Haseeb, Y.H. Wong, J. Mater. Sci. Mater. Electron. **6**(28), 4725 (2016)
52. C.-W. Yang, Y.-K. Fang, C.H. Chen, S.F. Chen, C.Y. Lin, C.S. Lin, M.F. Wang, Y.M. Lin, T.H. Hou, L.-G. Yao, Appl. Phys. Lett. **83**(2), 308 (2003)
53. Y.H. Wong, K.Y. Cheong, Electron. Mater. Lett. **8**(1), 47 (2012)
54. T. Kurniawan, Y.H. Wong, K.Y. Cheong, J.H. Moon, W. Bahng, K.A. Razak, Z. Lockman, H.J. Kim, N.-K. Kim, Mater. Sci. Semicond. Process. **14**(1), 13 (2011)
55. M.-K. Song, S.-W. Rhee, Thin Solid Films **492**(1), 19 (2005)
56. A. Hardy, S. Van Elshocht, J. D'Haen, O. Douhéret, S. De Gendt, C. Adelmann, M. Caymax, T. Conard, T. Witters, H. Bender, J. Mater. Res. **22**(12), 3484 (2007)
57. C.-H. Kao, T.C. Chan, K.S. Chen, Y.-T. Chung, W.-S. Luo, Microelectron. Reliab. **50**(5), 709 (2010)